Earth and Planetary Science Letters 493 (2018) 57–70

Contents lists available at ScienceDirect

Earth and Planetary Science Letters

www.elsevier.com/locate/epsl

Petrochronologic perspective on rhyolite volcano unrest at Laguna del Maule, Chile

Nathan L. Andersen [a,*], Brad S. Singer [a], Fidel Costa [b], John Fournelle [a], Jason S. Herrin [b,c], Gareth N. Fabbro [b]

[a] Department of Geoscience, University of Wisconsin-Madison, Madison, WI, 53706, United States of America
[b] Earth Observatory of Singapore, Nanyang Technological University, 639798, Singapore
[c] Facility for Analysis Characterization Testing and Simulation, Nanyang Technological University, 639798, Singapore

ARTICLE INFO

Article history:
Received 5 October 2017
Received in revised form 20 March 2018
Accepted 21 March 2018
Available online xxxx
Editor: T.A. Mather

Keywords:
rhyolite
Andes
diffusion timescales
plagioclase
trace elements
eruption trigger

ABSTRACT

Rhyolitic magmas have rarely erupted during historical times, thus we have a poor record of the signals of unrest that precede them. The Laguna del Maule volcanic field (LdM), Chile, is in the midst of a decade-long episode of unrest including surface inflation at more than 200 mm/yr. Geomorphic observations indicate that many similar deformation episodes occurred during the late Pleistocene and Holocene. During this time, approximately 40 km^3 of rhyolite has erupted effusively and explosively from at least 24 vents distributed around a 300 km^2 lake basin. The large volume, protracted eruptive history, and ongoing unrest of LdM offer an unusual opportunity to integrate petrologic reconstructions of recent rhyolite generation with geophysical and geodetic observations associated with an active, growing magma reservoir. New petrochronologic data shows that the most recent rhyolites, erupted during the last 3200 yr, each resided in the shallow crust for only decades following extraction from an underlying reservoir. The rhyolites contain only limited, cryptic evidence for magma replenishment and reheating in the form of Ba concentration spikes in plagioclase, which suggest biotite breakdown in a crystal-rich mush. The absence of evidence for substantial reheating or mixing with intruding magma preceding the rhyolitic eruptions indicates that they must have been triggered by another process. We propose the accumulation of fluids derived from the deeper degassing of mafic melts is capable of pressurizing eruptible magma bodies of low density rhyolite. This process likely continues to this day and is consistent with the best-fit models of the ongoing unrest. The striking absence of visible surface degassing accompanying the unrest at LdM suggests fluids are trapped beneath an impermeable carapace and could catalyze a future explosive eruption.

1. Introduction

Silicic magmatic systems can produce modest-to-large volume ($<$1–10^3 km^3) explosive eruptions and threaten regional population centers, infrastructure, and agriculture (Castro and Dingwell, 2009; Self and Blake, 2008; Sparks et al., 2005). In many settings, silicic magmas are thought to originate from a crystal mush—a crystalline framework containing $<$50% melt—assembled by shallow emplacement of magma over 10^4–10^5 yr (e.g., Hildreth, 2004). Gravity-driven processes such as compaction and hindered settling can extract rhyolitic melt from mush zones (Bachmann and Bergantz, 2004). In addition, the intrusion of hotter, less evolved magma, appears to be a fundamental catalyst of rhyolite generation and eruption by remelting solidified silicic material, mixing with and pressurizing pre-existing magma, and promoting the amalgamation of discrete, heterogeneous magma batches (e.g., Bachmann and Bergantz, 2006; Bindeman and Simakin, 2014; Bergantz et al., 2015, 2017; Huber et al., 2012; Burgisser and Bergantz, 2011; Charlier et al., 2008; Folch and Martí, 1998; Wolff et al., 2015). The time required to mobilize eruptible rhyolite from a long-lived magma reservoir is the subject of active investigations (e.g., Barker et al., 2016; Chamberlain et al., 2014; Druitt et al., 2012; Rubin et al., 2017; Singer et al., 2016; Till et al., 2015). Magma rejuvenation and eruption priming are commonly inferred to occur over months to centuries—timescales that are exceedingly short in geologic terms. However, in the context of volcano monitoring, lag times of months vs. centuries require substantially different approaches to assessing volcanic unrest when attempting to anticipate future eruptions.

* Corresponding author. Current address: University of Oregon, Department of Earth Sciences, Eugene, OR, 97403, United States of America.
E-mail address: nla@uoregon.edu (N.L. Andersen).

https://doi.org/10.1016/j.epsl.2018.03.043
0012-821X/

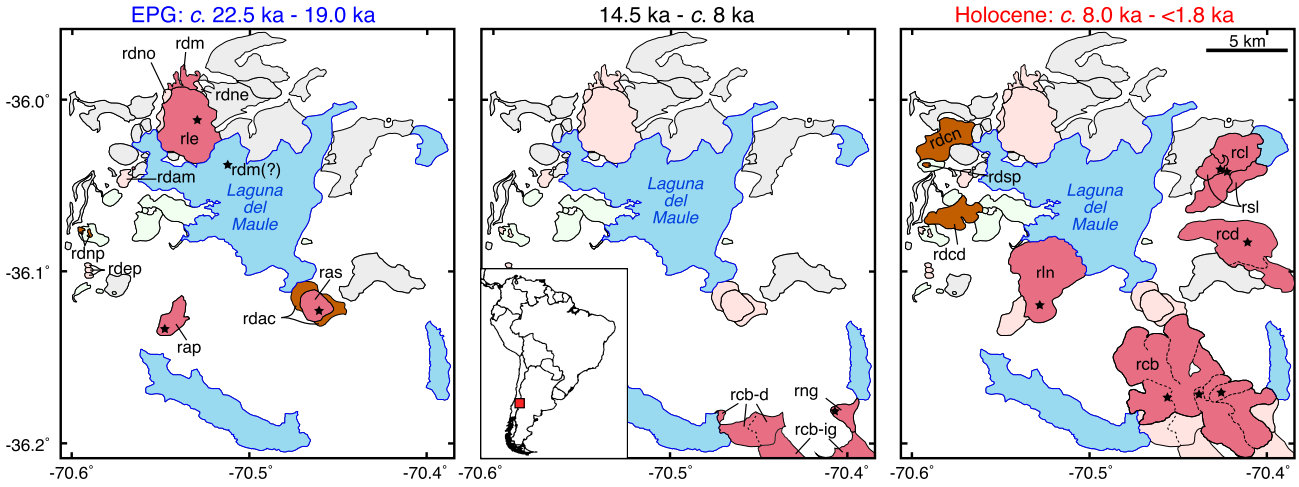

Fig. 1. Simplified geologic maps showing the locations of post-glacial silicic eruptions during the EPG period, the Holocene, and the interim (modified from Andersen et al., 2017; Hildreth et al., 2010). Post-glacial rhyolites, rhyodacites, and andesites are pink, orange, and green respectively. Units erupted prior to the most recent glacial retreat are light gray. Post-glacial silicic units erupted during an earlier period in the center and right panels are pale pink. The black stars mark the rhyolite-producing vents (Hildreth et al., 2010); the location of the vent for the EPG plinian *rdm* eruption within the modern lake is approximate (Fierstein, 2018). The red square in the inset shows the location of LdM in South America. (For interpretation of the colors in the figure(s), the reader is referred to the web version of this article.)

In the last 500 yr, only 65 silicic (dacite–rhyolite, trachydacite–trachyte, or phonolite) volcanoes have erupted worldwide, of which only 14 were dominantly rhyolitic, and only 3 (Pinatubo, Puyehue-Cordón Caulle, and St. Helens) were instrumentally monitored (Bignami et al., 2014; Jay et al., 2014; Newhall et al., 2017; Newhall and Punongbayan, 1996; Sherrod et al., 2008; Global Volcanism Program, 2013). This infrequent eruption of rhyolite magma limits our opportunities to integrate petrologic constraints with geophysical observations of volcano unrest. Consequently, forensic petrologic reconstruction of the processes that promoted late Pleistocene through historical eruptions provides a unique context for interpreting geophysical records of unrest (Barker et al., 2016; Jay et al., 2014; Singer et al., 2016; Wilson, 2017).

We present major and trace element compositions and textures of plagioclase and magnetite from rhyolite erupted in the currently restless Laguna del Maule volcanic field (LdM), located in the southern Andes at 36° S (Fig. 1; Hildreth et al., 2010; Singer et al., 2014). We interpret these data within a high resolution eruptive chronology (Andersen et al., 2017) to construct an integrated model of the compositional and physical evolution of the magma reservoir over 10^3–10^4 yr and quantify the tempo of processes preceding the most recent eruptions.

2. Geologic setting

LdM is situated 30 km behind the active volcanic front of the Southern Volcanic Zone (SVZ) of Central Chile. Since the most recent glacial retreat, locally at *c*. 23 to 19 ka based on $^{40}Ar/^{39}Ar$ dates of unglaciated lava flows (Singer et al., 2000; Andersen et al., 2017), volcanism at LdM has been dominantly silicic and concentrated within the central lake basin (Fig. 1; Andersen et al., 2017; Hildreth et al., 2010). Rhyolite eruptions at LdM were both effusive and explosive, and both eruptive styles yield products that contain less than 10% phenocrysts of plagioclase, biotite, and magnetite ± quartz ± amphibole. The frequency and spatial distribution of the post-glacial rhyolite eruptions at LdM were greatest during two pulses: an early post-glacial (EPG) period, 22.5–19 ka, and the middle to late Holocene (Fig. 1; Andersen et al., 2017). The EPG rhyolite eruptions began with the 20 km^3 plinian Rhyolite of Laguna del Maule, unit *rdm* (Fierstein, 2018), the large volume of which distinguishes it from the subsequent, smaller-volume (<3 km^3) rhyolites. Following an interim period during which rhyolite erupted only from the Barrancas complex in the southeastern lake basin (14.5–*c*. 8 ka), the focus of rhyolite volcanism expanded westward and northward during the Holocene, while also continuing within the Barrancas complex (Fig. 1; Andersen et al., 2017; Fierstein, 2018; Hildreth et al., 2010; Sruoga et al., 2017).

Rhyodacite and andesite eruptions also occurred throughout post-glacial times. However, they comprise a smaller cumulative volume (<5 km^3 total) than the rhyolites and were concentrated in the western LdM basin, away from the locus of rhyolite volcanism (Andersen et al., 2017; Hildreth et al., 2010). The rhyodacite lavas are distinguished from the rhyolites by higher crystallinities (10–20%), ubiquitous amphibole, and common cm-scale chilled mafic inclusions, which are nearly absent from the rhyolites (Andersen et al., 2017; Hildreth et al., 2010).

Geochemical, geochronologic, and geophysical investigations have produced insights into the structure and evolution of the LdM magma reservoir. Amphibole barometry, trace element compositions, and radiogenic isotope ratios indicate the rhyolite erupted at LdM was produced in the shallow crust (Andersen et al., 2017). This shallow magmatism is the uppermost expression of a multi-tiered magma system involving two distinct domains of crustal assimilation. Partial melting occurred both within the stability field of garnet (≥1.2 GPa; Rapp and Watson, 1995) and at lower pressure via garnet-free dehydration melting of amphibole-bearing crust. The depth of this second zone is not well constrained, but it notably does not involve older metamorphic and intrusive basement with highly radiogenic Sr and Pb isotope ratios (Andersen et al., 2017).

The lack of mafic to intermediate eruptions within the locus of rhyolite volcanism is hypothesized to reflect the interception of mafic magma by a voluminous shallow silicic magma reservoir (Hildreth et al., 2010). All rhyolites have similar whole-rock chemistry, but the Holocene rhyolites are subtly enriched in middle rare earth elements (MREE) and Y relative to those erupted during the EPG period. Andersen et al. (2017) propose that this distinction indicates multiple physically discrete batches of crystal-poor rhyolite were extracted from a longer-lived, crystal-rich reservoir through time.

Since 2007, surface uplift at LdM measured by InSAR and continuous GPS has exceeded 200 mm/yr and continues at the time of writing (Feigl et al., 2014; Fournier et al., 2010; Le Mével et al., 2015). The best-fit source of this deformation is an inflating sill at a depth of ~5 km; a model of coupled time-varying magma injection and reservoir pressurization reproduces 7.3 yr of sur-

face deformation by the intrusion of 0.19–0.37 km^3 of magma (Le Mével et al., 2016). A negative Bouguer gravity anomaly is spatially coincident with the center of uplift. Miller et al. (2017b) model this feature as a 30 km^3 body at 2–4 km depth with a density of 1800–1900 kg/m^3, interpreted as rhyolitic magma containing exsolved fluid and <50% crystals, contained within a 115 km^3 reservoir of crystal-rich magma. Moreover, surface wave tomography has identified a several-hundred km^3 low velocity zone spanning 1.5 to 7 km depth surrounding the Bouguer gravity and deformation sources, consistent with a shallow mush zone (Wespestad, 2017). Superimposed on these inferred domains of partial melt are shallow (1.5–2.0 km depth) mass changes detected by 4D microgravity consistent with the infiltration of hydrothermal brine along faults and fractures, possibly induced by an increase in permeability due to seismic activity (Miller et al., 2017a). Despite these signs of ongoing magmatic activity, there is a striking lack of visible surface degassing at LdM, which often accompanies significant periods of volcanic unrest (e.g., Barberi et al., 1984; Hill et al., 2003; Parks et al., 2013). The LdM basin is ringed by a paleoshoreline left behind following the breaching of a lava dam and drawdown of the lake highstand at 9.4 ka (Hildreth et al., 2010; Singer et al., 2018). A GPS survey of this feature shows the southern portion is uplifted >60 m relative to the northern segments. This deformation is attributed to the addition of >20 km^3 of magma to the shallow crust during the Holocene (Singer et al., 2018).

3. Methods summary

We undertook textural and chemical analysis of plagioclase crystals from eight rhyolites: the EPG units *rap*, *ras*, *rle*, and *rdm* and Holocene units *rcb*, *rcd*, *rln*, and *rsl*. Approximately 1100 rhyolite plagioclase phenocrysts were characterized by optical and backscattered electron (BSE) imaging. The compositions of a representative subset were determined by electron microprobe (EPMA: SiO_2, Al_2O_3, FeO, CaO, Na_2O, and K_2O) and laser ablation inductively-coupled plasma mass spectrometry (LA-ICP-MS: Mg, Ti, Sr, Ba, Rb, Ce, and La). We measured the compositions of 9 to 23 crystals per unit including core-to-rim compositional traverses (20–100 µm spot spacing) and spot analyses, totaling 593 spots. Compositional transects for diffusion modeling were measured at greater spatial resolution (3–4 µm by EPMA, 10 µm by LA-ICP-MS) on eight crystals from the Holocene rhyolite eruptions comprising the range of textures observed. In addition, the plagioclase populations of the EPG *rdne* and *rdno* and Holocene *rdcd* and *rdcn* rhyodacite lavas, were characterized with coarse traverses (20–50 µm spot spacing) across 8–12 crystals, totaling 1022 spots. Although the number of crystals analyzed per unit was not exhaustive, care was taken to pick representative crystals and traverses to ensure comparisons among the crystal populations of each unit are meaningful. Additional analytical details are in the supplementary materials.

4. Mineral textures and compositions

The plagioclase in each of the rhyolites have similar textural and compositional characteristics. The dominant crystal population (90%) is broadly homogeneous with An contents of An_{20}–An_{35} [An = 100 × Ca/(Na+Ca+K), molar]. Within this compositional range, subtle normal zoning is common; a subgroup of this population (20%) contains minor oscillatory zoning superimposed on an overall decrease in An content from core to rim. Crystals containing more distinct normal zonation are uncommon (10%) and contain cores of up to An_{51} mantled by rims of An_{20}–An_{30}. Reversely zoned crystals are rare (<1%), with interiors of An_{17}–An_{20} mantled by rims of An_{20}–An_{30}. The rhyodacite plagioclase crystals are more calcic (An_{20}–An_{60}, predominantly >An_{30}; Supplementary Fig. A1) and range in texture from homogeneous to complexly zoned with sieved cores and resorption surfaces. The trace element compositions of all plagioclase crystals vary regularly with An content: the concentrations of Ti, Mg, and Sr increase whereas those of Ba, Rb, La, and Ce decrease with increasing An content (Fig. 2).

Andersen et al. (2017) report magnetite-ilmenite thermometry of LdM lavas. Here, we examine the major and minor element compositions (TiO_2, Al_2O_3 Fe_2O_3, FeO, MgO, and MnO) of magnetite in greater detail as an additional tracer of the thermochemical continuity of the post-glacial eruptions. Magnetite crystals in both the rhyodacites and rhyolites are compositionally and texturally unzoned, with ulvöspinel contents of Ulv_{13}–Ulv_{25} [Ulv = 100 × (1 − Fe^{3+})/(Fe^{3+} + 2 × Ti–Mn); molar]. Minor elements vary consistently with TiO_2: MgO and Al_2O_3 increase and MnO decreases.

5. Mineral records of magmatic processes

5.1. Magma storage conditions and volatile contents

Magnetite-ilmenite thermometry yields temperatures of 760–850 °C and 796–854 °C for the rhyolites and rhyodacites, respectively, and oxygen fugacities (fO_2) 1.2–1.3 log units above the Ni–NiO buffer (Andersen et al., 2017; Frost, 1991). Amphibole is absent from most LdM rhyolites; in the rhyodacites, amphibole crystals in apparent equilibrium with the host magma based on the calculated equilibrium melt SiO_2 composition (Putirka, 2016) yield temperatures of 828–933 °C and pressures of 180–250 MPa (Andersen et al., 2017). Water contents calculated by plagioclase hygrometry for most rhyolites and rhyodacites are 4.4–6.0 wt.% indicating they would be water-saturated between 140 and 200 MPa (Waters and Lange, 2015; Newman and Lowenstern, 2002), a similar range to that indicated by amphibole barometry (Fig. 3).

5.2. Plagioclase record of magma evolution

Relating mineral and melt compositions requires knowledge of the mineral-melt partitioning behavior; plagioclase partitioning is dependent on both the temperature and An content, which in turn varies with temperature, host melt composition, and volatile content. We considered several parameterizations of this relationship (Bédard, 2006; Bindeman et al., 1998; Dohmen and Blundy, 2014), but all are hampered by a paucity of experiments involving low-An plagioclase and high-SiO_2 melts. To assess the applicability of these models to the LdM system, we calculated an apparent partition coefficient for each plagioclase laser spot. The crystallization temperature and host melt composition were estimated using Rhyolite-MELTS fractional crystallization models (hereafter referred to as MELTS; version 1.2; Gualda et al., 2012) and regressions of the whole-rock trace element data (see the electronic supplement for details). The apparent partition coefficients show some scatter and offset from the models, however most are generally consistent with the predicted variations with An and temperature (Supplemental Fig. A2). The Rb partitioning is substantially offset below all of the models, and thus its behavior is not well constrained. Based on the comparison with the apparent partition coefficients, we have adopted the models of Bindeman et al. (1998) for K, Mg, Ba, and Ti, Bédard (2006) for La and Ce, and Dohmen and Blundy (2014) for Sr in all of our calculations. Although the model of Bédard (2006) is the best match for the light rare earth element (LREE) data, it does not reproduce the bimodality at low An observed at LdM. We discuss factors that may affect the behavior of the LREE in section 5.3.

The calculated melt concentrations of Sr, Mg, Ti, and K reproduce the variations of the intermediate to silicic whole-rock com-

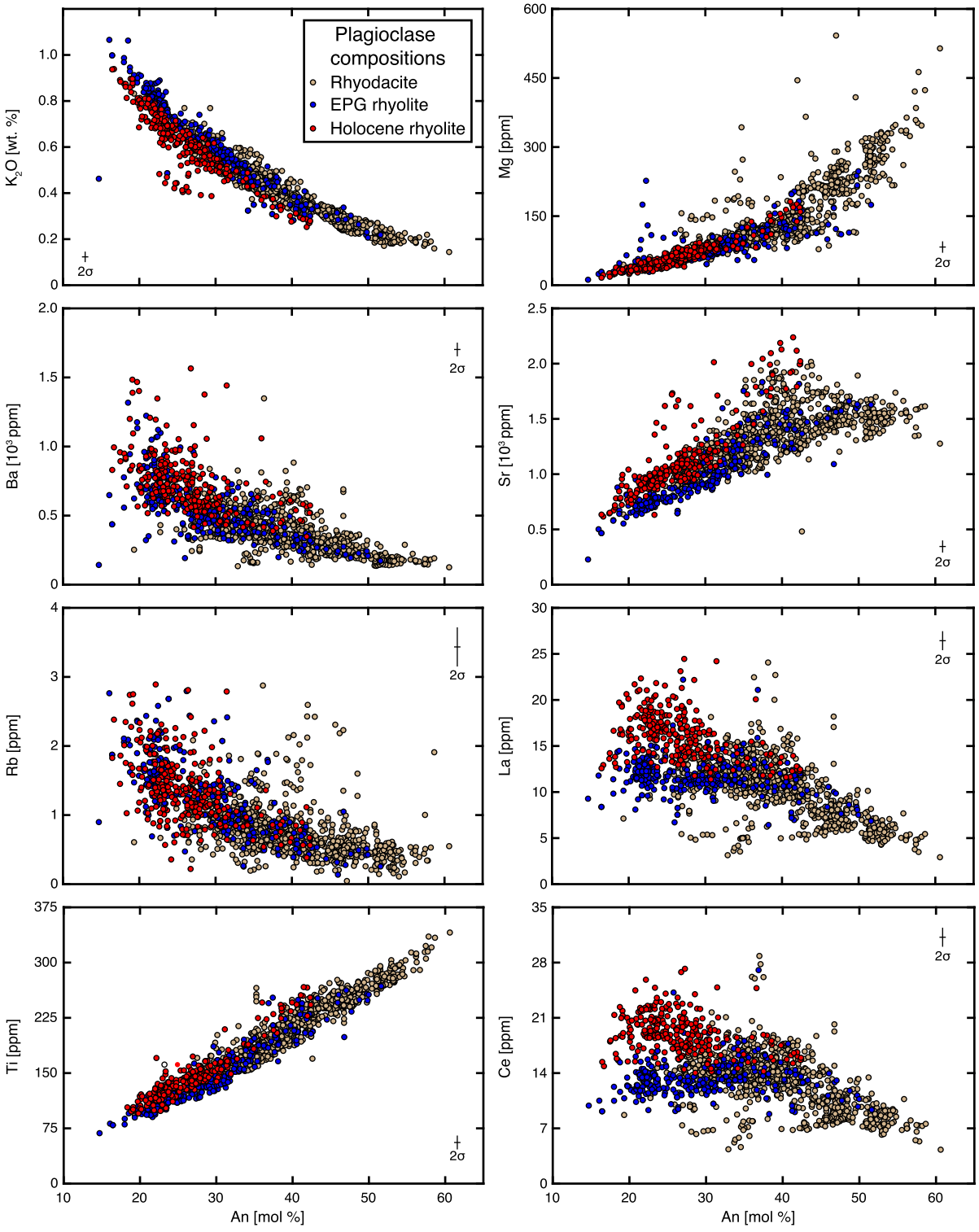

Fig. 2. The variation of trace element compositions with An content for the LdM rhyolite and rhyodacite plagioclase crystals. Crosses show the typical 2σ analytical uncertainties. The An and K_2O contents were measured by EPMA and all other elements by LA-ICP-MS.

positions (Andersen et al., 2017; Hildreth et al., 2010) but span small compositional gaps in the whole-rock data (Fig. 4). The LREE and Ba are decoupled from these elements and are discussed in sections 5.3 and 5.4. The calculated melt compositions indicate that the texturally complex rhyodacite plagioclase grew from andesitic to rhyolitic melt (Fig. 4). This compositional diversity, along with the mafic inclusions in the rhyodacite lavas and deformation of the paleoshoreline, is consistent with the repeated intrusion of magma during post-glacial times (Andersen et al., 2017; Singer et al., 2018).

In contrast, this process imparted little petrologic fingerprint to the rhyolites. Recharge of extant magma reservoirs may be recorded by reversely-zoned pyroxene and feldspar crystals with rims enriched in Sr, Mg, and Ti (e.g., Barker et al., 2016; Singer et al., 2016; Till et al., 2015). However, the rhyolite plagioclase crystals display the opposite trend. Moreover, rhyolite generated by re-

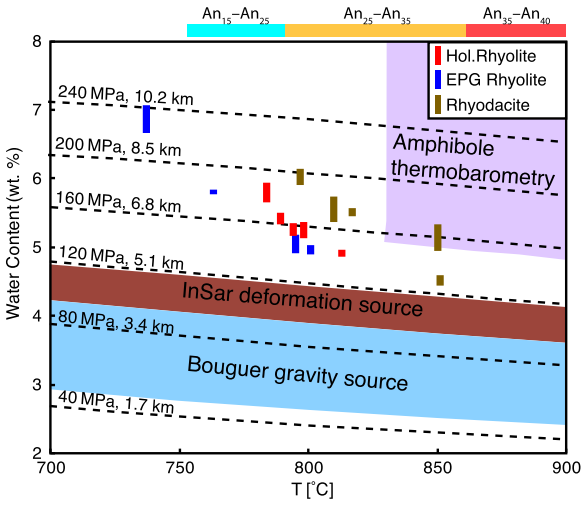

Fig. 3. The water contents of LdM rhyolite and rhyodacite lavas calculated from plagioclase rim and whole-rock compositions using plagioclase-glass hygrometry (Waters and Lange, 2015) plotted against the average Fe–Ti oxide temperatures of the host rock (Andersen et al., 2017). The dashed contours are water saturation isobars calculated using VolatileCalc (Newman and Lowenstern, 2002); depth in the crust is calculated assuming an average density of 2400 kg/m^3. The uncertainties in the water contents include those associated with the Fe–Ti oxide thermometer (±30 °C). The fields show the range of pressures indicated by amphibole barometry of the LdM rhyodacites (Andersen et al., 2017) and the modeled sources of ground deformation and the Bouguer gravity anomaly (Feigl et al., 2014; Miller et al., 2017b). The bars above the panel show the crystallization temperatures predicted by the preferred MELTS simulation (see the supplementary materials) for plagioclase with An contents of An_{15} to An_{40}. The MELTS model includes an assumed initial water content and therefore this estimated An-temperature relationship was not used in the plagioclase hygrometry calculations.

mobilizing near- to sub-solidus material would likely yield greater intra-crystal compositional and isotopic diversity than observed at LdM (Bindeman and Simakin, 2014; Chamberlain et al., 2014; Charlier et al., 2008; Till et al., 2015). The uniformly low An-contents and limited trace element variation of the rhyolite plagioclase, which reflects the rhyolite whole-rock data (Fig. 4), support a scenario of primarily closed system crystallization. Rhyolites erupted in the Valley of Ten Thousand Smokes and at Taupo Volcano during the Holocene similarly lack a record of magma recharge despite co-erupted intermediate magma, or subsequent rhyolites that clearly record this process (Singer et al., 2016; Barker et al., 2016). Plagioclase compositions $<An_{25}$ are abundant in the LdM rhyolites, but are nearly absent from the rhyodacites (Fig. 4; Supplementary Fig. A1). Thus, we conclude the rhyolite plagioclase population primarily grew following the segregation of crystal-poor rhyolite magma from the larger crystalline magma reservoir.

5.3. *Temporally evolving magmatic fingerprints*

The compositions of Fe–Ti oxides re-equilibrate in only days to weeks at magmatic temperatures (e.g., Devine et al., 2003; Tomiya et al., 2013), making them an excellent tracer of co-magmatic volcanic products such as vent-proximal and distal fall deposits (e.g., Fierstein, 2007). Here, the LdM magnetite compositions are used to assess if rhyolite eruptions distributed around the lake basin were fed by a single, crystal-poor magma body. Magnetite records variable pre-eruption thermo-chemical conditions for the *rdm*, smaller-volume EPG, and Holocene rhyolites (Fig. 5). This compositional fingerprint illustrates a transition from cooler, higher-SiO_2 rhyolite during the EPG (74–76% wt.% SiO_2; 737–801 °C), to warmer, lower-SiO_2 rhyolite (72–75% wt.% SiO_2; 780–857 °C) during the Holocene (Andersen et al., 2017; Hildreth et al., 2010).

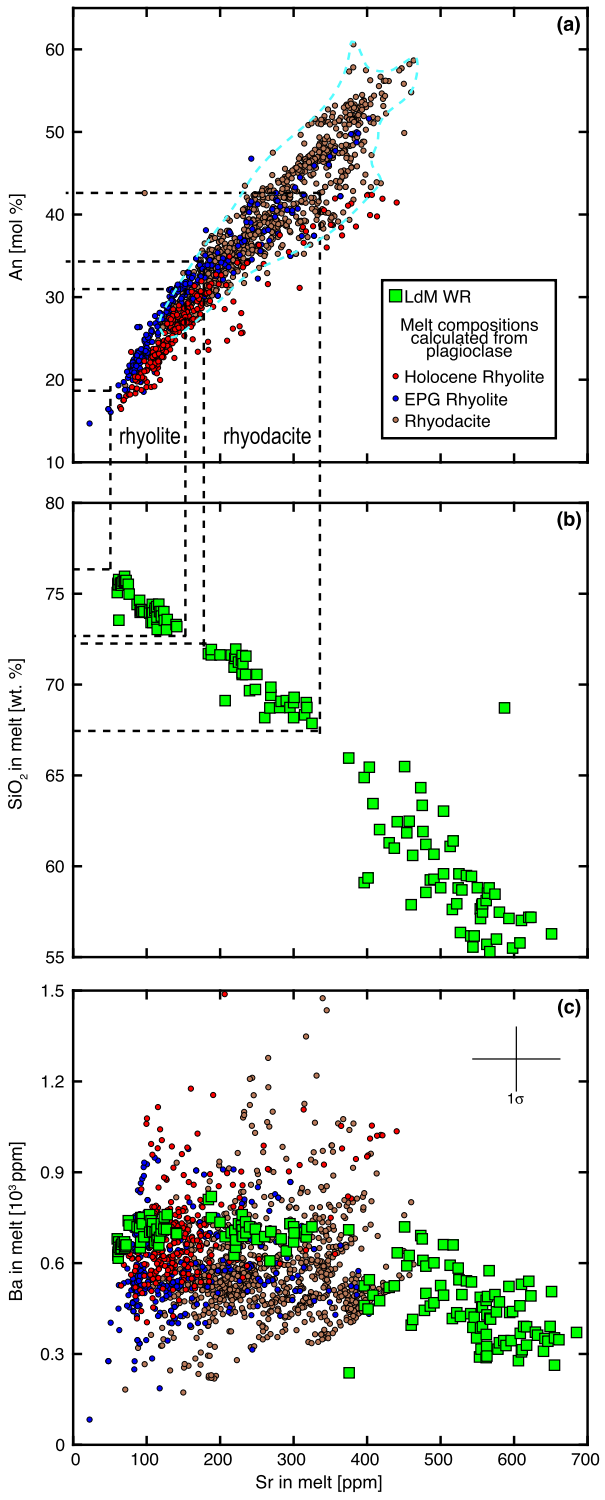

Fig. 4. (a) and (b) Correlation of plagioclase and whole-rock (WR) compositions. Melt compositions calculated from the plagioclase data record significant inheritance of phenocrysts derived from more evolved melt in the rhyodacites (the partially obscured rhyodacite data is outlined by the light blue dashed line), but limited entrainment of rhyodacite plagioclase into the rhyolite magma batches. (c) Comparison of the central LdM whole-rock and calculated Ba melt compositions. The greater scatter in the Ba data compared to the other trace elements likely reflects local variability in biotite stability in response to magma recharge. The crosses show the typical 1σ uncertainty of the melt calculation including the precision of the plagioclase analysis and the confidence interval of the partition coefficient model parameters (Dohmen and Blundy, 2014; Bindeman et al., 1998). The calculated melt compositions of additional trace elements are shown in Supplementary Fig. 5. Whole-rock data are from Andersen et al. (2017) and Hildreth et al. (2010).

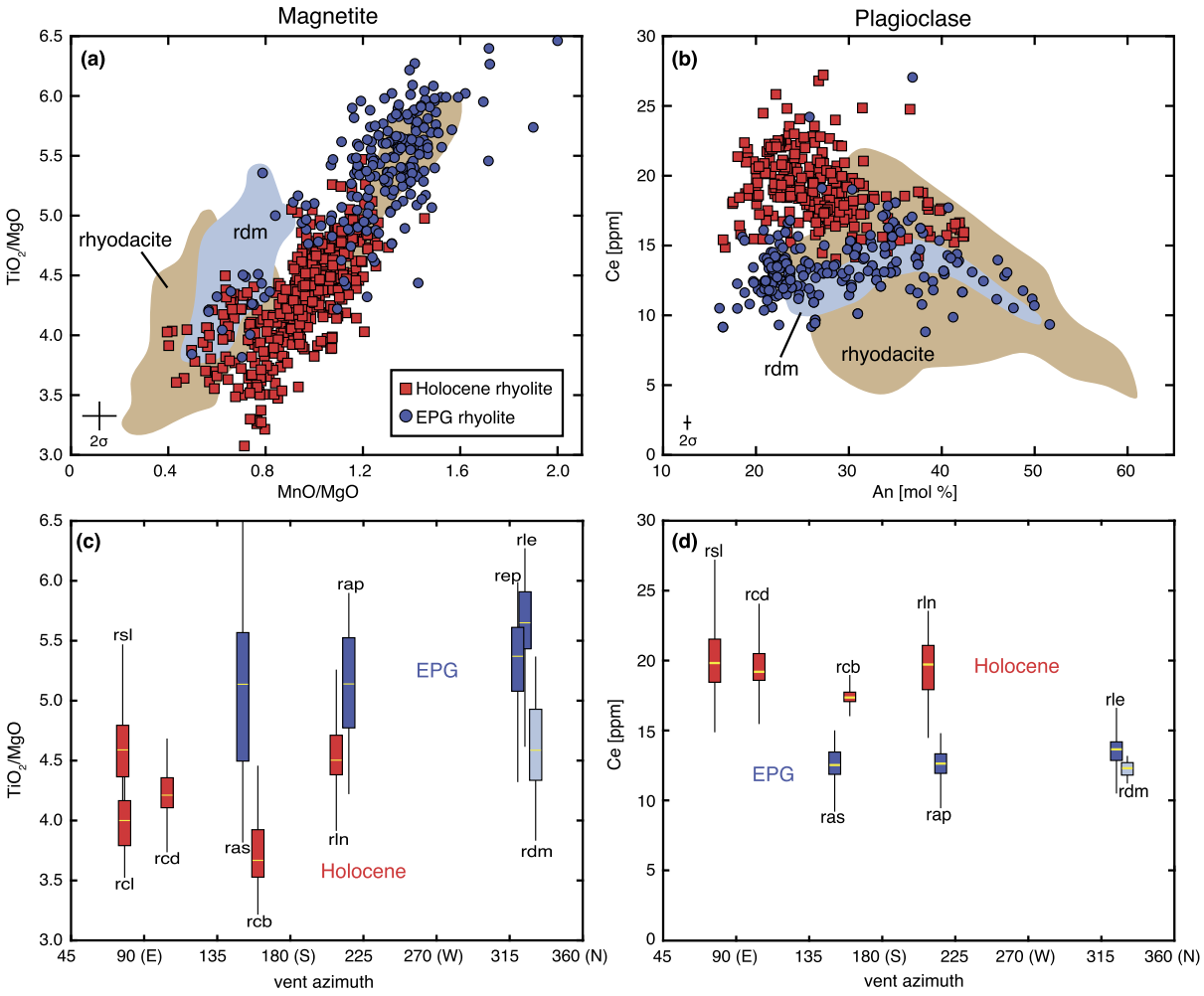

Fig. 5. Compositional fingerprints of rhyolite magma batches. (a) The minor element compositions of LdM rhyolite and rhyodacite magnetite crystals. Distinct compositional groups reflect the changing pre-eruption thermochemical conditions of the rhyolite batches erupted through time. (b) The Ce composition of rhyolite and rhyodacite plagioclase phenocrysts. The bimodality of Ce at low An contents illustrates distinct magma production regimes during EPG and Holocene times and that there was little physical interaction between the earlier and later erupted rhyolites. The brown fields are data from the rhyodacites and the blue fields are for the EPG plinian *rdm* eruption. (c) and (d) The spatial distribution of the compositionally contrasting rhyolites. The x-axis shows the azimuth to the vent for each eruption measured from the center of the lake. The filled boxes encompass the 25th–75th percentiles of the data for each unit, the tails show the 5th–95th, and the yellow lines mark the median. The footprint of the EPG and Holocene vents overlap (Fig. 1), but the compositions of the rhyolites erupted during each of these periods are more similar than those issued at different times from vents in close proximity.

In contrast to the magnetite compositions that quickly re-equilibrate to changing magmatic conditions, the relatively slow diffusion of major elements and trace elements such as Ba, Ti, and the REE in plagioclase preserves varied compositions and textures that comprise a complementary record of the evolving magma system (e.g., Charlier et al., 2008; Singer et al., 1995; Smith et al., 2009). The plagioclase LREE compositions are bimodal at low An contents: for example, the Holocene rhyolite plagioclase crystals are distinguished from those of the EPG eruptions by Ce contents greater than 15 ppm (Fig. 5). A similar contrast in REE compositions distinguishes the Pleisocene Therasia and Cape Riva dacites erupted at Santorini (Fabbro et al., in press). There the plagioclase compositions mirror contrasts in the whole-rock chemistry. However, at LdM the contrast between the Holocene and EPG rhyolite plagioclase LREE compositions is not consistent with the narrow range of whole-rock compositions (La: 30–35 ppm, Ce: 56–67 ppm; Andersen et al., 2017). Consequently, the plagioclase compositions likely reflect a difference in partitioning behavior. Volatiles, particularly halogens (F, Cl), can inhibit the partitioning of trace elements into crystallizing phases by increasing the availability of sites for REE in the melt, forming REE-halogen complexes, or producing a fluid with high affinity for trace elements (Fleet and Pan, 1997; Ponader and Brown, 1989; Lowenstern, 1993). Whereas there is not yet halogen data for the LdM silicic magmas to corroborate this hypothesis, variations in the halogen content of the LdM magma system could contribute to the contrasting plagioclase REE compositions.

Regardless of their uncertain source, the distinct compositional populations of low-An plagioclase demonstrate that the Holocene rhyolites did not incorporate significant material from the EPG eruptions. Thus, the earlier rhyolite must have erupted completely, or any residual magma had limited interaction with the active magma reservoir. The plagioclase and magnetite compositions indicate that at least three distinct batches of crystal-poor rhyolite were segregated to produce the *rdm*, modest-volume EPG, and Holocene rhyolites. However, their consistency within the EPG and Holocene groups is permissive of a single crystal-poor magma body producing multiple eruptions. Intercalated tephra deposits consistent with simultaneous eruption (e.g., Pistolesi et al., 2016) have not been located at LdM (Fierstein, 2018). Consequently, this scenario would require incubation of the crystal-poor magma body for centuries to millennia. We examine magma residence times of the rhyolites in section 6 to further explore this possibility.

5.4. Cryptic record of magma recharge

In contrast to the simple evolution indicated by most elements in the rhyolite plagioclase, the zoning patterns and concentrations of Ba reveal a subtle history of more complex thermochemical interactions between the extracted rhyolite and recharge magmas. Narrow zones (<60 μm) within plagioclase are enriched in Ba, consistent with melt compositions up to nearly twice those of the whole-rock (Fig. 4, Supplementary Fig. A6). These zones are occasionally associated with subtle increases in Sr or An content, however Ba is largely decoupled from the other elements. Large changes in Ba concentration in the melt are likely controlled by the stability of Ba-rich phases. In the absence of sanidine, biotite is the most significant Ba sink in the LdM magma system. Biotite-melt partition coefficients for Ba range from 5–29 (Nash and Crecraft, 1985; Rollinson, 1993) and thus biotite in equilibrium with an average LdM silicic lava (680 ppm Ba) would have a Ba concentration of 3400–19700 ppm. The decomposition of biotite crystals, which can begin below 800 °C (Patiño Douce and Beard, 1995; Singh and Johannes, 1996), would produce halos of Ba-enrichment that could be recorded by nearby plagioclase crystals. It would require mixing of less than 15% of the melt derived from biotite dehydration with typical LdM silicic magma to achieve a melt composition >1000 ppm, consistent with the Ba-enriched plagioclase domains. The rarity and narrow width of these plagioclase domains and the homogeneous whole-rock Ba compositions of the LdM silicic lavas (Andersen et al., 2017; Hildreth et al., 2010) suggests biotite destabilization did not produce large quantities of melt, but rather was a local effect that was subsequently homogenized into the larger magma body (e.g., Bachmann et al., 2014). We interpret the high variance of Ba throughout the range of An contents as a chemical signature of magma recharge affecting both the mush and crystal-poor domains of the magma reservoir (Fig. 4c).

6. Timescales of rhyolite magma residence

The relative timing and rate of magmatic processes are needed to connect past eruptions to geophysical records of unrest. Cation diffusion in crystals is increasingly employed to explore these timescales (e.g. Barker et al., 2016; Chamberlain et al., 2014; Druitt et al., 2012; Matthews et al., 2012; Rubin et al., 2017; Singer et al., 2016; Till et al., 2015). We focus on three late Holocene rhyolites (Fig. 1; *rsl*, 3.2±1.2 ka; *rcd*, 2.2 ± 1.3 ka; and *rln*, <1.8 ± 0.9 ka; Andersen et al., 2017), in order to compare the processes that catalyzed the most recent eruptions to those driving the current unrest.

Whereas the narrow intra-plagioclase compositional range of the Holocene rhyolites does not obviously record magma mixing or reheating, the compositions of crystal interiors are not in equilibrium with those of the rims or host rock (Fig. 6). The timescales over which diffusion relaxes this compositional gradient can yield estimates of the duration of plagioclase residence at magmatic temperatures (Costa et al., 2003). We interpret these crystal residence times to be the duration of pre-eruption storage of crystal-poor rhyolite following its segregation from the larger magma reservoir.

6.1. Trace element diffusion model

We modeled Mg diffusion in plagioclase using the temperature- and An-dependent diffusion coefficient of Van Orman et al. (2014), the partition coefficient of Bindeman et al. (1998), and a finite difference solution to the equations of Costa et al. (2003). Diffusion was modeled at the average Fe–Ti oxide temperature of each unit (789°–800 °C; Andersen et al., 2017). An profiles for the model calculations with a constant spot spacing of ~2.5 μm were generated by linear interpolation between adjacent EPMA spots. We assumed a constant composition of the host melt at the crystal rim and a symmetric diffusion profile across a plane perpendicular to the crystal section at the core. The choice of inner boundary condition, symmetric profile vs. fixed composition, does not have a significant impact on the timescales. The similar geometries of the An, Mg, Sr, and Ti profiles, despite the significantly different diffusion rates of these elements (Costa and Morgan, 2011), indicate little diffusive equilibration has taken place and the gradients primarily reflect growth zonation. Thus, a step function initial condition is not appropriate (Supplemental Fig. A9; Chamberlain et al., 2014; Druitt et al., 2012; Till et al., 2015). We utilized an approach similar to Druitt et al. (2012), whereby the initial Mg profile was calculated based on the compositional relationships among the plagioclase An content and Sr and Mg in the whole-rock samples, which given their low crystallinities are reasonable estimates of the liquid compositions. First a curve was fit to the An and Sr magma compositions calculated from the Holocene plagioclase data. The associated melt Mg content was then calculated from the correlation between the whole-rock Sr and Mg compositions (Supplementary Fig. A7). Finally, the initial plagioclase Mg composition was calculated using the mineral-melt partition coefficient.

This approach is dependent on the MELTS simulations and partitioning models approximating the magma conditions during plagioclase crystallization. These assumptions could be violated if the MELTS calibration is not appropriate for LdM or if kinetic effects during crystallization perturb the predicted equilibrium behavior of Sr and Mg. The close correlation of the melt compositions calculated from plagioclase and the whole-rock data indicates that these effects are minimal. Moreover, utilizing slower-diffusing Ti in place of Sr in initial condition calculation yields similar profiles, which further indicates that this procedure produces geologically meaningful initial conditions. Equilibrium profiles are calculated at the Fe–Ti oxide temperature for each unit using the melt composition calculated for the crystal rim. In all cases, the small difference between this profile and one constructed using the whole-rock composition does not impact our interpretations.

The calculation of the initial condition, temperature, and its effect on the diffusion coefficient contribute to the uncertainty of the model timescales. We have used a ±30 °C uncertainty associated with the Fe–Ti oxide temperatures, which at the temperature of interest corresponds to a factor of two uncertainty in the model timescales. Variations of the initial conditions can have potentially large impact on the model timescale because of the limited extent of re-equilibration. Propagation of the uncertainties associated with the partition coefficient models, data regressions, and chemical analysis produce 1σ uncertainties of the initial profiles of 12–37%, which correspond to a factor of 2–3 difference in the model timescales.

Sr diffusion was modeled using the same numerical routine to corroborate the Mg timescales and to validate the use of Sr to calculate the initial Mg profile. The expression of Giletti and Shanahan (1997) for An_{27} was used to calculate the temperature-dependent diffusion coefficient. The initial condition was taken as the measured Sr profile. The diffusion distance of Sr produced by the Mg model timescales is negligible and thus limited reequilibration of the Sr concentrations occurred.

6.2. Timescales of rhyolite extraction and residence

The model timescales of all plagioclase crystals from units *rsl* and *rln* are not well constrained because the calculated initial profiles are within uncertainty of the measured Mg compositions. The preservation of disequilibrium in these crystals nevertheless indicates little diffusion has occurred. The maximum residence time of these phenocrysts is taken to be that required for the modeled

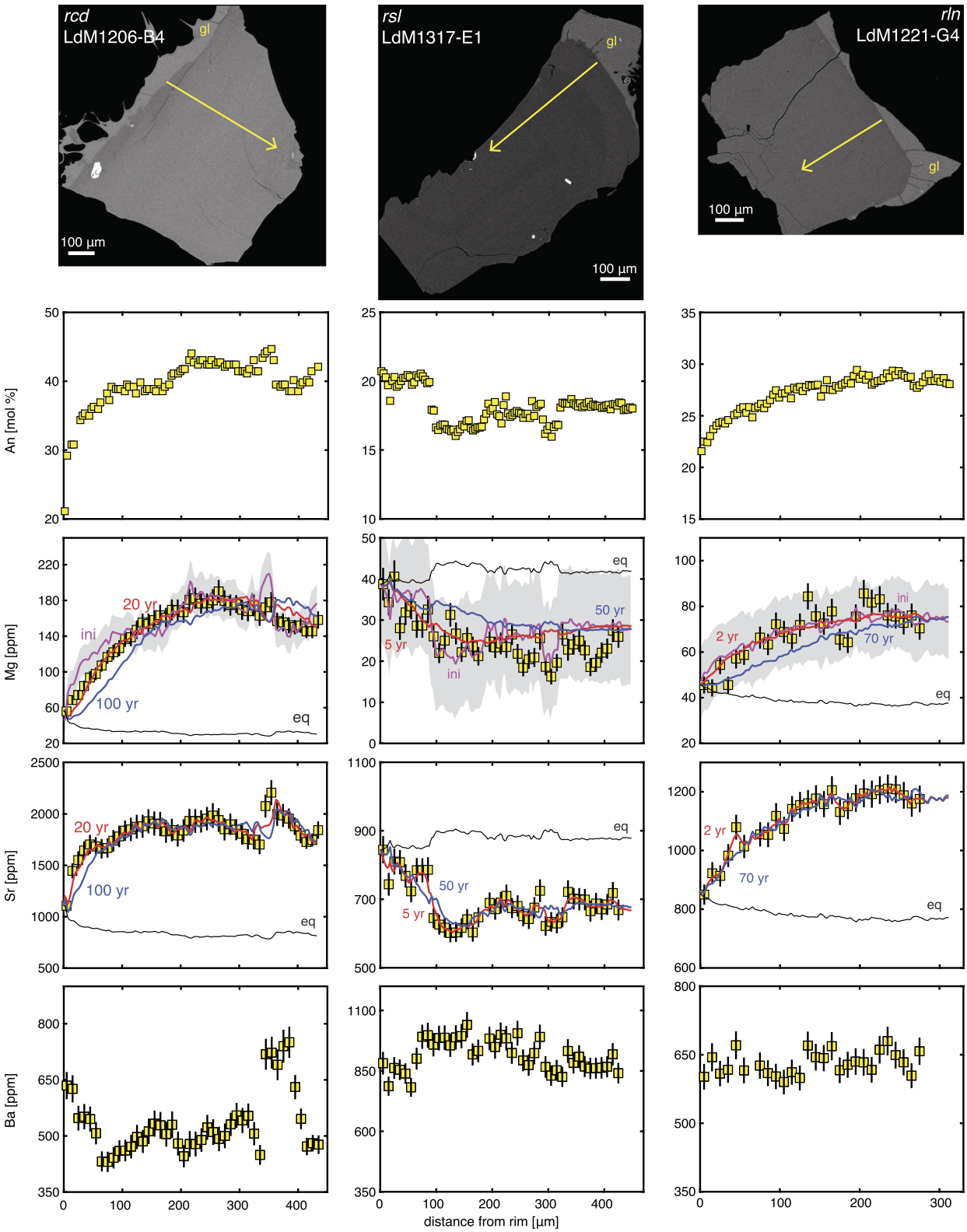

Fig. 6. Representative BSE images and diffusion timescales for LdM plagioclase crystals from units *rcd*, *rsl*, and *rln*; images and models for all crystals are available in Supplementary Fig. A8. The arrows show the locations of the EPMA and LA-ICP-MS traverses. The initial Mg profile (ini, pink line) is estimated based on the compositions of less-mobile Sr and An. The solid red line shows the best fit model for each measured profile (yellow boxes with 2σ analytical uncertainties) and the blue curves show the effect of longer magma residence; the model timescale for each line is labeled in the same color. Profiles showing concentrations in equilibrium with the outermost rim of each crystal are shown in black. The light gray fields show the 1σ confidence interval of the initial profile. Grain boundaries are identified by the presence of adhering matrix glass (gl).

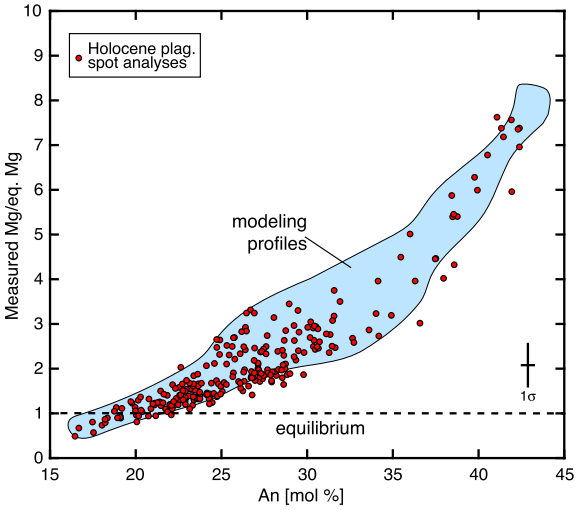

Fig. 7. Comparison of the crystals used for diffusion modeling to the Holocene rhyolite plagioclase population characterized by spot EPMA and LA-ICP-MS analysis. The y-axis is the ratio of the Mg concentration measured in the plagioclase to that in equilibrium with the host-rock based on the Fe–Ti oxide temperature and the partitioning model of Bindeman et al. (1998). The disequilibrium recorded in the compositional profiles used for the model timescales (light blue field) is consistent with that of the aggregate Holocene plagioclase population.

Mg profile to fall outside of the analytical uncertainty of the measured profile, and ranges from 5 to 100 yr (Fig. 6). Two *rcd* crystals are more distinctly zoned, with interiors up to An_{45}, consistent with rare plagioclase crystallized in dacitic to rhyodacitic magma and entrained during rhyolite segregation. These crystals yield better constrained models and timescales of 5 and 20 yr, which are within the range of maximum residence times derived from the more homogeneous crystals (Fig. 6).

To evaluate whether these timescales are representative of the entire crystal population, we calculated the deviation from equilibrium with the host rock for all the rhyolite plagioclase spot analyses. Intra-crystal disequilibrium is common for compositions $>An_{25}$ and its extent increases with An content; the modeled profiles are consistent with this trend (Fig. 7). An contents greater than An_{35} are uncommon, but typically mantled by rims similar in composition to the dominant homogeneous, low-An plagioclase crystal population. This compositional continuity indicates all crystals experienced similar conditions during the decades leading up to eruption.

Tephrochronology indicates the eruptions of *rsl*, *rcd*, and *rln* occurred over a period of centuries to several millennia (Fierstein, 2018); the overlapping uncertainties of the $^{40}Ar/^{39}Ar$ eruption ages are consistent with this interpretation, but are not sufficiently precise to calculate meaningful repose times (Andersen et al., 2017). The similar plagioclase and magnetite compositions suggest these eruptions could have tapped a common magma body. However, the ubiquitous intra-crystal disequilibrium in plagioclase would not survive several thousand years of storage at high temperature. Thus, either these crystals were cooled rapidly following each eruption and were remobilized into the next (e.g., Cooper and Kent, 2014) or each of these eruptions was produced by a separate, ephemeral magma body with nearly identical composition. The absence of EPG rhyolite plagioclase in the Holocene eruptions, mineral textures consistent with repeated cycles of rejuvenation and solidification, and compositions depleted in Sr and Ba by extensive feldspar crystallization in the rhyolites favor the extraction of discrete magma batches associated with each eruption.

Moreover, if each eruptive episode left behind residual magma, remobilization of this growing volume of material by subsequent eruptions would become increasingly likely through the late Pleistocene and Holocene. Accordingly, with the recognition that the dynamics that control the proportion of extracted melt that is erupted are enigmatic, we propose that the majority of each segregated batch of rhyolite is vented during eruption and explore a triggering mechanism that favors this scenario in the next section. With the exception of the EPG *rdm* plinian eruption, no rhyolite eruption at LdM has exceeded 3 km^3 (Fierstein, 2018; Hildreth et al., 2010; Sruoga et al., 2017). Within our proposed framework, the temperature and composition of the source mush were buffered by frequent magma recharge such that batches of nearly identical rhyolite could be repeatedly extracted, briefly stored, and erupted but the accumulated crystal-poor magma present at any time during the Holocene never appreciably exceeded the erupted volumes.

7. Towards the integration of petrologic constraints with the geophysical record of unrest

The petrochonologic and geophysical findings provide a variety of lenses through which to interpret the configuration and processes of the LdM magma reservoir. The ongoing inflation and deformed paleoshoreline indicate the modern unrest is only the most recent of many episodes of shallow magma emplacement, which have enlarged and sustained the LdM magma system during post-glacial times (Le Mével et al., 2016; Singer et al., 2018). The low-density (1800–1900 kg/m^3) body revealed by the Bouguer gravity survey requires the presence a fluid phase. Miller et al. (2017b) propose that this phase is derived from closed system exsolution. However, this model decouples the source of the Bouguer gravity anomaly from the spatially coincident surface inflation. In the following discussion, we suggest an alternative source of pre-eruption fluid, explore the physical significance of the geophysical observations in the context of the petrochronologic data, and propose a physical model that integrates these perspectives of the LdM magma system.

7.1. The source and effect of exsolved fluid

Closed system fluid exsolution may be catalyzed by decompression or cooling and crystallization that yields fluid-oversaturated residual melt. Fluid may also be derived externally from the volatiles released by hydrous mafic to intermediate magma ascending from depth. The accumulation of such fluids has been proposed to account for volcanic gas emissions in excess of that dissolved in the erupted magma (Cashman, 2004; Edmonds et al., 2010; Métrich et al., 2009; Parmigiani et al., 2016; Shinohara, 2008; Wallace, 2001). We used MELTS (Gualda et al., 2012) to explore the physical scenarios required to produce a low-density magma reservoir. Miller et al. (2017b) utilized a similar approach but focused on a rhyolitic bulk composition. However, the short plagioclase timescales suggest accumulations of crystal-poor rhyolite were ephemeral features. A crystal mush of dacitic bulk composition containing interstitial rhyolitic melt, is a more likely state for long-term storage (e.g., Cooper and Kent, 2014; Hildreth, 2004; Rubin et al., 2017).

Table 1 shows the range of parameters considered by the MELTS models. An initial magma with a rhyolitic or dacitic composition was cooled from the liquidus to 750 °C to predict the relationships among temperature, pressure, crystal content, exsolved fluid content, and the density of a magma reservoir residing in the shallow crust. External fluid addition was approximated by specifying initial water contents in excess of fluid saturation; its potential source and volume is discussed below. Densities of 1800–1900 kg/m^3 for the three-phase (melt, crystals, and fluid) system are achieved in both the open- and closed-system simulations by high volume fractions of fluid, 16–32 vol.% (2.5–5 wt.%; vol.% = 100 × vol. fluid/[vol. fluid+vol. melt+vol. crystals]; wt.% =

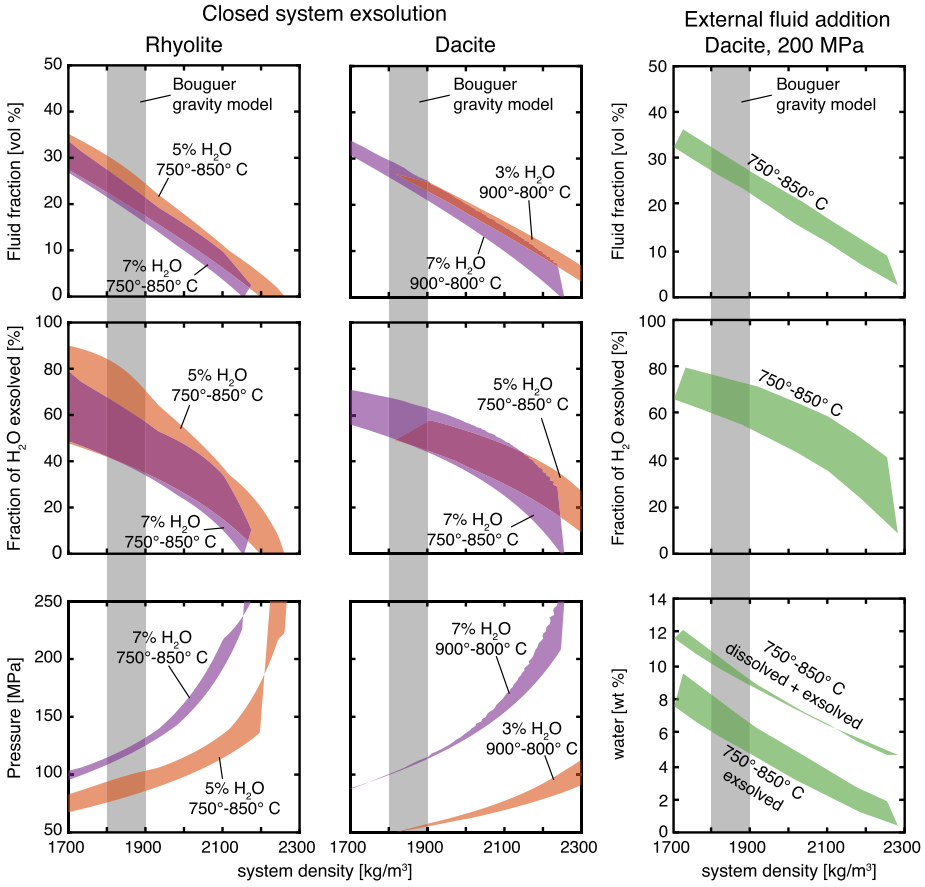

Fig. 8. The results of MELTS simulations exploring closed system fluid exsolution and external fluid addition; the model parameters are in Table 1. The low densities of the Bouguer gravity model (1800–1900 kg/m^3) are achieved by fluid volume fractions greater than 25%, which correspond to the exolution of more than half of the total H_2O in the system. Closed system exsolution achieves densities <1900 kg/m^3 only at pressures less than 130 MPa, which is inconsistent with the LdM mineral data. Plots of additional model outputs are available in Supplemental Fig. A11.

Table 1
Parameters used in the MELTS simulations to estimate the effect of a fluid phase.

	Internal exsolution		External fluxing[c]
Initial composition[a]	Rhyolite	Dacite	Dacite
T [°C]	850–750	900–800	750–850
P [MPa]	250–50	250–50	200
H_2O [wt.%]	5–7	3–7	4–12
fO_2 buffer	QFM+2[b]	QFM+2	QFM+2

[a] Units *rln* and *dlp* (Andersen et al., 2017; Hildreth et al., 2010) are taken as representative of LdM rhyolite and dacite, respectively.
[b] Two log units above the quartz-fayalite-magnetite buffer.
[c] The effects of external fluid addition are estimated by specifying initial water contents in excess of fluid saturation.

100 × wt. fluid/[wt. fluid+wt. melt+wt. crystals]). Whereas densities <1900 kg/m^3 at fluid fractions <20 vol.% only occur in the models of rhyolitic bulk composition, the range of fluid fractions required in all the simulations to produce the densities inferred for the gravity anomaly broadly overlap (Fig. 8). It is notable that the melt fractions at which these densities were achieved ranged from 15% to 65%, highlighting that at high fluid fractions the system density is relatively insensitive to the melt fraction and bulk composition of the magma. Our simulations of closed system exsolution agree with those of Miller et al. (2017b) in that system densities <1900 kg/m^3 are achieved only by magmas containing >4 wt.% initial H_2O at low pressure; for example, <90 MPa for 5 wt.% H_2O (Fig. 8). The external fluid addition simulations achieve densities of 1800–1900 kg/m^3 at total water contents of 9–11 wt.%, which corresponds to the addition of 3–5 wt.% fluid to an already fluid-saturated magma reservoir (Fig. 8).

Closed system fluid exsolution can theoretically produce a low-density magma reservoir consistent with the Bouguer anomaly. However, several characteristics of the mineral data argue against this scenario. Amphibole barometry yields crystallization pressures of 180–250 MPa (Andersen et al., 2017), which is at least twice those suggested by the closed-system simulations. Moreover, closed system exsolution implies the ascent of fluid saturated melt from greater depth, >150 MPa for water contents >5 wt.%. The dominantly homogeneous plagioclase populations of the LdM rhyolites are not consistent with this decompression path over which more than half of the volatile content may be exsolved (Supplementary Fig. A12; Newman and Lowenstern, 2002). Thus, the exsolution of a large volume of fluid due to closed system, low-pressure storage and crystallization would be a substantial departure from the processes operative at LdM during post-glacial times. We prefer external fluxing as the more significant source of pre-eruption fluid.

Studies of volcanic gas emissions, melt inclusions, and phase equilibria indicate that SVZ mafic magmas contain up to 4 wt.% H_2O and 2500 ppm CO_2 (Rea, 2009; Shinohara and Witter, 2005; Wallace, 2005; Watt et al., 2013). Basaltic andesite magma with 3 wt.% H_2O and a density of 2500 kg/m^3 contains 7.5 × 10^{10} kg H_2O/km^3, which corresponds to 0.2 km^3 of exsolved fluid, assuming a fluid density of 400 kg/m^3 (Supplementary Fig. 11). Le Mével et al. (2016) model the ongoing deformation as the result of magma emplacement at 0.025–0.050 km^3/yr, depending on the compressibility. This episode, or several similar episodes that occur over decades, could supply a flux of fluid that is volumetri-

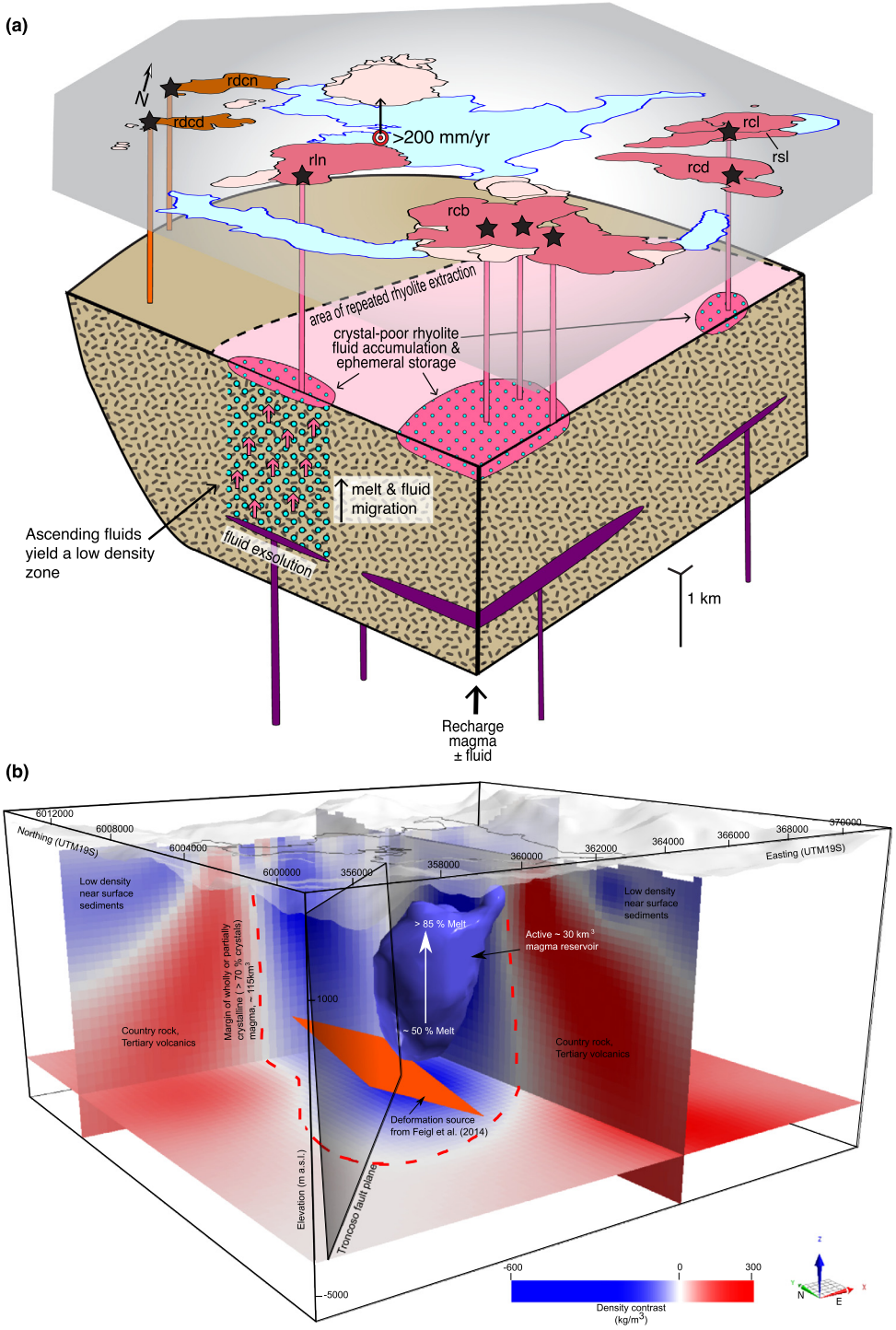

Fig. 9. Comparison of geophysical and petrologic models of LdM. (a) Schematic diagram, with a 5× vertical exaggeration, of our preferred model of the crystal-rich magma system underlying the active Holocene vents (stars). Map unit fill colors are the same as Fig. 1. The bullseye and vertical arrow is the approximate center of ongoing uplift at >200 mm/yr (Feigl et al., 2014; Le Mével et al., 2015). During the Holocene, modest-volume batches of compositionally similar rhyolite (dark pink bodies) were repeatedly extracted from a broad spatial footprint within the crystalline LdM magma reservoir (light pink area). The accumulation and eruption of rhyolite is catalyzed by fluids derived from ascending magma. This fluid flux would contribute to low density zones within the magma reservoir. (b) The model of the source of the low Bouguer gravity anomaly proposed by Miller et al. (2017b) is a 30 km^3 body, interpreted as rhyolite containing <50% crystals, that extends from approximately 4–2 km depth. This melt-rich body is contained within a 115 km^3 highly crystalline magma reservoir. Although exsolved volatiles play an integral role in the LdM magma system, we suggest the volume of fluid required to achieve the low density (1800–1900 kg/m^3) of this feature is not realistic for a large magma body, which suggests the gravity measurements are influenced by a shallow hydrothermal system or fluid-rich roof zone of the magma reservoir.

cally substantial relative to the modest eruptive volumes typical of LdM (<3 km^3). Additionally, the MELTS simulations consider only a pure H_2O volatile phase. The flux of CO_2-rich fluid derived from mafic magma would lower the solubility of H_2O in the melt and thereby catalyze fluid exsolution and crystallization (e.g., Métrich et al., 2009). Isobaric solubility calculations performed using VolatileCalc (Newman and Lowenstern, 2002) at 800 °C and 200 MPa predict a linear decrease in the dissolved H_2O content of fluid-saturated rhyolite of 0.3 wt.% per additional 100 ppm dissolved CO_2, up to 1000 ppm (Supplementary Fig. A12).

A 30 km^3 magma body with density <1900 kg/m^3 would require a fluid volume >7.5 km^3, corresponding to the fluid content of at least 37 km^3 of mafic magma, greater than the magma volume estimated to drive the Holocene paleoshoreline deformation (Singer et al., 2018). This large volume fraction of pre-eruptive fluid also exceeds that inferred for magma reservoirs that fed several highly explosive eruptions. It is as much as 40% greater than that of the Bishop Tuff, 2–3 times that of the Kos Plateau Tuff, and as much as 4 times that of the 1991 eruption of Pinatubo (Bachmann et al., 2010; Gerlach et al., 1996; Wallace et al., 1995). Moreover, 30 vol.% fluid represents a theoretical maximum at which point the formation of channels prevents the further accumulation of exsolved volatiles and such concentrations are often inferred only in the upper reaches of magma reservoirs (Cashman, 2004; Wallace, 2001). In this context, storage of 30 km^3 of magma containing sufficient fluid to produce a density <1900 kg/m^3 appears to be unrealistic. However, given the magnitude of the Bouguer gravity anomaly, we do not discount the broader conclusion of Miller et al. (2017b) of the presence of fluid in the LdM magma reservoir. Instead, we suggest that shallow hydrothermal fluids, such as those inferred by Miller et al. (2017a) from 4D microgravity, may have contributed to an underestimate of the depth and density of the LdM magma system and additionally that transient external fluid addition could produce local low-density magmatic domains.

7.2. An integrated physical model

Despite likely being present in smaller volumes than proposed by Miller et al. (2017b), we suggest exsolved fluid nevertheless plays an integral role in promoting rhyolite volcanism at LdM. Recent fluid dynamic models of bubble migration and accumulation suggest fluid forms fast-transport channels in crystal-rich mush at a lower volume fraction (20% vs 30%) than in less crystalline magma (Parmigiani et al., 2016; Wallace, 2001). In this case, volatiles exsolved from mafic magma would rapidly traverse the lower reaches of the magma reservoir, but stall in segregated bodies of crystal-poor rhyolite. Given a sufficient flux, this accumulating fluid would produce a critical overpressure and trigger an eruption (Fig. 9; Parmigiani et al., 2016; Singer et al., 2016). This flux of hot volatiles would more efficiently heat the mush than conductive heat transfer, and small-scale remelting and fracturing could enhance the rate of melt extraction (Bachmann and Bergantz, 2006; Huber et al., 2011). Following a recharge event, 10–15 vol.% fluid may also become trapped in the mush producing a persistent low-density zone (Christopher et al., 2015; Parmigiani et al., 2016).

A physical record of a pre-eruptive fluid phase is not commonly obvious in the products of volcanic eruptions. A focused study of melt inclusions hosted in LdM crystals is the subject of future work; however, initial observations have found neither abundant vapor bubbles within melt inclusions nor discrete fluid inclusions that would directly record the pre-eruption fluid. Nevertheless, the similarly cryptic records of pre-eruptive magma rejuvenation at LdM, Katmai, and Taupo suggests that volatile-induced overpressure may be an important mechanism whereby magmatic rejuvenation can trigger eruptions, particularly in large, repeatedly active silicic systems, without mingling of the extant and intruding magmas. At LdM, the fluid flux associated with the magma recharge that drives ground deformation contributes to a shallow low-density zone and likely promoted the repeated, rapid segregation and eruption of crystal-poor rhyolite during the Holocene (Fig. 9).

8. Summary and conclusions

Geophysical and petrologic approaches each provide a partial, but complementary, view of a pre-eruptive magma reservoir. The ongoing and Holocene records of deformation and the outcrop- to mineral-scale textures of the rhyodacitic lavas record repeated, shallow interaction between mafic and silicic magma beneath LdM. Yet, this process has left sparse evidence in the rhyolites. Instead, trace element disequilibrium preserved in plagioclase records the years- to decades-long process of rhyolite melt segregation. Geodetic and gravity observations today find the ongoing addition of magma to the upper crust and the presence of a fluid phase, respectively, that likely catalyzed past liquid–crystal separation and eruption. The lack of visible surface degassing at LdM may reflect ongoing fluid accumulation within a pressurizing magma reservoir and a brewing explosive eruption. Similar cryptic records of interaction between recharge and extant magmas at LdM and other silicic volcanic systems suggests external fluid addition is an underappreciated eruption catalyst. An improved capability to recognize and estimate the volume of pre-eruption exsolved fluid in the petrologic record and models that couple three-phase magma dynamics to signals accessible by geophysical monitoring would allow for better integration of these observations, comparison between past eruptions and modern unrest, and hazard assessment at restless volcanic systems.

Acknowledgements

Allison Rubin is thanked for analytical assistance during the 2014 LA-ICP-MS session. This work greatly benefited from many fruitful discussions with Hélène Le Mével, Judy Fierstein, and the LdM research group. Christy Till and an anonymous reviewer are thanked for thorough and constructive comments and Tamsin Mather for editorial handling. This research is supported by the US NSF (EAR-1322595, EAR-1411779 to BSS) and an NSF East Asia and Pacific Summer Institutes fellowship to NLA (1414759). BSS is grateful for an appointment as a Visiting Professor at EOS-NTU during which the 2015 LA-ICP-MS session was completed. FC research was supported by a National Research Foundation Investigatorship Award (NRF-NRFI2017-06).

Appendix A. Supplementary material

Supplementary material related to this article can be found online at https://doi.org/10.1016/j.epsl.2018.03.043.

References

Andersen, N.L., Singer, B.S., Jicha, B.R., Beard, B.L., Johnson, C.M., Licciardi, J.M., 2017. Pleistocene to Holocene growth of a large upper crustal rhyolitic magma reservoir beneath the active Laguna del Maule volcanic field, central Chile. J. Petrol. 58, 85–114. https://doi.org/10.1093/petrology/egx006.

Bachmann, O., Bergantz, G.W., 2006. Gas percolation in upper-crustal silicic crystal mushes as a mechanism for upward heat advection and rejuvenation of near-solidus magma bodies. J. Volcanol. Geotherm. Res. 149, 85–102. https://doi.org/10.1016/j.jvolgeores.2005.06.002.

Bachmann, O., Bergantz, G.W., 2004. On the origin of crystal-poor rhyolites: extracted from batholithic crystal mushes. J. Petrol. 45, 1565–1582. https://doi.org/10.1093/petrology/egh019.

Bachmann, O., Deering, C.D., Lipman, P.W., Plummer, C., 2014. Building zoned ignimbrites by recycling silicic cumulates: insight from the 1000 km^3 Carpenter Ridge Tuff, CO. Contrib. Mineral. Petrol. 167, 1–13. https://doi.org/10.1007/s00410-014-1025-3.

Bachmann, O., Wallace, P.J., Bourquin, J., 2010. The melt inclusion record from the rhyolitic Kos Plateau Tuff (Aegean Arc). Contrib. Mineral. Petrol. 159, 187–202. https://doi.org/10.1007/s00410-009-0423-4.

Barberi, F., Corrado, G., Innocenti, F., Luongo, G., 1984. Phlegraean fields 1982–1984: brief chronicle of a volcano emergency in a densely populated area. Bull. Volcanol. 47, 175–185. https://doi.org/10.1007/BF01961547.

Barker, S.J., Wilson, C.J.N., Morgan, D.J., Rowland, J.V., 2016. Rapid priming, accumulation, and recharge of magma driving recent eruptions at a hyperactive caldera volcano. Geology. https://doi.org/10.1130/G37382.1.

Bédard, J.H., 2006. Trace element partitioning in plagioclase feldspar. Geochim. Cosmochim. Acta 70, 3717–3742. https://doi.org/10.1016/j.gca.2006.05.003.

Bergantz, G.W., Schleicher, J.M., Burgisser, A., 2015. Open-system dynamics and mixing in magma mushes. Nat. Geosci. 8, 793–796. https://doi.org/10.1038/ngeo2534.

Bergantz, G.W., Schleicher, J.M., Burgisser, A., 2017. On the kinematics and dynamics of crystal-rich systems: hydrogranular dynamics. J. Geophys. Res., Solid Earth 122, 6131–6159. https://doi.org/10.1002/2017JB014218.

Bignami, C., Corradini, S., Merucci, L., De Michele, M., Raucoules, D., De Astis, G., Stramondo, S., Piedra, J., 2014. Multisensor satellite monitoring of the 2011 Puyehue-cordon Caulle eruption. IEEE J. Sel. Top. Appl. Earth Obs. Remote Sens. 7, 2786–2796. https://doi.org/10.1109/JSTARS.2014.2320638.

Bindeman, I.N., Davis, A.M., Drake, M.J., 1998. Ion microprobe study of plagioclase-basalt partition experiments at natural concentration levels of trace elements. Geochim. Cosmochim. Acta 62, 1175–1193.

Bindeman, I.N., Simakin, A.G., 2014. Rhyolites – hard to produce, but easy to recycle and sequester: integrating microgeochemical observations and numerical models. Geosphere 10, 930–957. https://doi.org/10.1130/GES00969.1.

Burgisser, A., Bergantz, G.W., 2011. A rapid mechanism to remobilize and homogenize highly crystalline magma bodies. Nature 471, 212–215. https://doi.org/10.1038/nature09799.

Cashman, K.V., 2004. Volatile controls on magma ascent and eruption. In: State of the Planet: Frontiers and Challenges in Geophysics, vol. 150, pp. 109–124.

Castro, J.M., Dingwell, D.B., 2009. Rapid ascent of rhyolitic magma at Chaitén volcano, Chile. Nature 461, 780–783. https://doi.org/10.1038/nature08458.

Chamberlain, K.J., Morgan, D.J., Wilson, C.J.N., 2014. Timescales of mixing and mobilisation in the Bishop Tuff magma body: perspectives from diffusion chronometry. Contrib. Mineral. Petrol. 168, 1–24. https://doi.org/10.1007/s00410-014-1034-2.

Charlier, B.L.A., Wilson, C.J.N., Davidson, J.P., 2008. Rapid open-system assembly of a large silicic magma body: time-resolved evidence from cored plagioclase crystals in the Oruanui eruption deposits, New Zealand. Contrib. Mineral. Petrol. 156, 799–813. https://doi.org/10.1007/s00410-008-0316-y.

Christopher, T.E., Blundy, J., Cashman, K., Cole, P., Edmonds, M., Smith, P.J., Sparks, R.S.J., Stinton, A., 2015. Crustal-scale degassing due to magma system destabilization and magma-gas decoupling at Soufrière Hills Volcano, Montserrat. Geochem. Geophys. Geosyst. 16, 2797–2811. https://doi.org/10.1002/2015GC005791.

Cooper, K.M., Kent, A.J.R., 2014. Rapid remobilization of magmatic crystals kept in cold storage. Nature 506, 480–483. https://doi.org/10.1038/nature12991.

Costa, F., Chakraborty, S., Dohmen, R., 2003. Diffusion coupling between trace and major elements and a model for calculation of magma residence times using plagioclase. Geochim. Cosmochim. Acta 67, 2189–2200. https://doi.org/10.1016/S0016-7037(00)01345-5.

Costa, F., Morgan, D., 2011. Time constraints from chemical equilibration in magmatic crystals. In: Dosseto, A., Turner, S., Van Orman, J.A. (Eds.), Timescales of Magmatic Processes: from Core to Atmosphere, pp. 125–159.

Devine, J.D., Rutherford, M.J., Norton, G.E., Young, S.R., 2003. Magma storage region processes inferred from geochemistry of Fe ± Ti oxides in andesitic magma, Soufrière Hills Volcano, Montserrat, W.I. J. Petrol. 44, 1375–1400.

Dohmen, R., Blundy, J., 2014. A predictive thermodynamic model for element partitioning between plagioclase and melt as a function of pressure, temperature and composition. Am. J. Sci. 314, 1319–1372. https://doi.org/10.2475/09.2014.04.

Druitt, T.H., Costa, F., Deloule, E., Dungan, M., Scaillet, B., 2012. Decadal to monthly timescales of magma transfer and reservoir growth at a caldera volcano. Nature 482, 77–80. https://doi.org/10.1038/nature10706.

Edmonds, M., Aiuppa, A., Humphreys, M., Moretti, R., Giudice, G., Martin, R.S., Herd, R.A., Christopher, T., 2010. Excess volatiles supplied by mingling of mafic magma at an andesite arc volcano. Geochem. Geophys. Geosyst. 11, 1–16. https://doi.org/10.1029/2009GC002781.

Fabbro, G., Druitt, T., Costa, F., in press. Storage and eruption of silicic magma across the transition from dominantly effusive to caldera-forming states at an arc volcano (Santorini, Greece). J. Petrol. https://doi.org/10.1093/petrology/egy013.

Feigl, K.L., Le Mével, H., Tabrez Ali, S., Córdova, L., Andersen, N.L., DeMets, C., Singer, B.S., 2014. Rapid uplift in Laguna del Maule volcanic field of the Andean southern volcanic zone (Chile) 2007–2012. Geophys. J. Int. 196, 885–901. https://doi.org/10.1093/gji/ggt438.

Fierstein, J., Postglacial eruptive history established by mapping and tephra stratigraphy provides perspectives on magmatic system beneath Laguna del Maule, Chile, Presented at: AGU Chapman Conference on Merging Geophysical, Petrochronologic, and Modeling Perspectives of Large Silicic Magma Systems, Quinamavida, Chile, 2018.

Fierstein, J., 2007. Explosive eruptive record in the Katmai region, Alaska Peninsula: an overview. Bull. Volcanol. 69, 469–509. https://doi.org/10.1007/s00445-006-0097-y.

Fleet, M.E., Pan, Y., 1997. Rare earth elements in apatite: uptake from H_2O-bearing phosphate-fluoride melts and the role of volatile components. Geochim. Cosmochim. Acta 61, 4745–4760. https://doi.org/10.1016/S0016-7037(97)00292-5.

Folch, A., Martí, J., 1998. The generation of overpressure in felsic magma chambers by replenishment. Earth Planet. Sci. Lett. 163, 301–314. https://doi.org/10.1016/S0012-821X(98)00196-4.

Fournier, T.J., Pritchard, M.E., Riddick, S.N., 2010. Duration, magnitude, and frequency of subaerial volcano deformation events: new results from Latin America using InSAR and a global synthesis. Geochem. Geophys. Geosyst. 11, Q01003. https://doi.org/10.1029/2009GC002558.

Frost, B.R., 1991. Introduction to oxygen fugacity and its petrologic importance. Rev. Mineral. Geochem. 25, 1–10.

Gerlach, T.M., Westrich, H.R., Symonds, R.B., 1996. Preeruption vapor in magma of the climactic Mount Pinatubo eruption: source of the giant stratospheric sulfur dioxide cloud. In: Newhall, C.G., Punongbayan, R.S. (Eds.), Fire and Mud: Eruptions and Lahars of Mount Pinatubo, Philippines. University of Washington Press, Seattle, pp. 415–433.

Giletti, B., Shanahan, T., 1997. Alkali diffusion in plagioclase feldspar. Chem. Geol. 1, 3–20.

Global Volcanism Program, 2013. Volcanoes of the World, v. 4.6.2, Venzke, E. (Ed.). Smithsonian Institution. https://doi.org/10.5479/si.GVP.VOTW4-2013. Accessed 31 May 2017.

Gualda, G.A.R., Ghiorso, M.S., Lemons, R.V., Carley, T.L., 2012. Rhyolite-MELTS: a modified calibration of MELTS optimized for silica-rich, fluid-bearing magmatic systems. J. Petrol. 53, 875–890. https://doi.org/10.1093/petrology/egr080.

Hildreth, W., 2004. Volcanological perspectives on Long Valley, Mammoth Mountain, and Mono Craters: several contiguous but discrete systems. J. Volcanol. Geotherm. Res. 136, 169–198. https://doi.org/10.1016/j.jvolgeores.2004.05.019.

Hildreth, W., Godoy, E., Fierstein, J., Singer, B.S., 2010. Laguna del Maule volcanic field: eruptive history of a Quaternary basalt to rhyolite distributed volcanic field on the Andean range crest in central Chile. Servicio Nacional de Geologia y Mineria, Bolletin 63.

Hill, D.P., Langbein, J.O., Prejean, S., 2003. Relations between seismicity and deformation during unrest in Long Valley Caldera, California, from 1995 through 1999. J. Volcanol. Geotherm. Res. 127, 175–193. https://doi.org/10.1016/S0377-0273(03)00169-0.

Huber, C., Bachmann, O., Dufek, J., 2011. Thermo-mechanical reactivation of locked crystal mushes: melting-induced internal fracturing and assimilation processes in magmas. Earth Planet. Sci. Lett. 304, 443–454. https://doi.org/10.1016/j.epsl.2011.02.022.

Huber, C., Bachmann, O., Dufek, J., 2012. Crystal-poor versus crystal-rich ignimbrites: a competition between stirring and reactivation. Geology 40, 115–118. https://doi.org/10.1130/G32425.1.

Jay, J., Costa, F., Pritchard, M., Lara, L., Singer, B., Herrin, J., 2014. Locating magma reservoirs using InSAR and petrology before and during the 2011–2012 Cordon Caulle silicic eruption. Earth Planet. Sci. Lett. 395, 254–266. https://doi.org/10.1016/j.epsl.2014.03.046.

Le Mével, H., Feigl, K.L., Córdova, L., Demets, C., Lundgren, P., 2015. Evolution of unrest at Laguna del Maule volcanic field (Chile) from InSAR and GPS measurements, 2003 to 2014. Geophys. Res. Lett. 42, 6590–6598. https://doi.org/10.1109/36.662741.Pitz.

Le Mével, H., Gregg, P.M., Feigl, K.L., 2016. Magma injection into a long-lived reservoir to explain geodetically measured uplift: application to the 2007–2014 unrest episode at Laguna del Maule volcanic field, Chile. J. Geophys. Res., Solid Earth 121, 6092–6108. https://doi.org/10.1002/2016JB013066.

Lowenstern, J.B., 1993. Evidence for a copper-bearing fluid in magma erupted at the Valley of Ten Thousand Smokes, Alaska. Contrib. Mineral. Petrol. 114, 409–421. https://doi.org/10.1007/BF01046542.

Matthews, N.E., Huber, C., Pyle, D.M., Smith, V.C., 2012. Timescales of magma recharge and reactivation of large silicic systems from Ti diffusion in quartz. J. Petrol. 53, 1385–1416. https://doi.org/10.1093/petrology/egs020.

Métrich, N., Bertagnini, A., Di Muro, A., 2009. Conditions of magma storage, degassing and ascent at Stromboli: new insights into the volcano plumbing system with inferences on the eruptive dynamics. J. Petrol. 51, 603–626. https://doi.org/10.1093/petrology/egp083.

Miller, C.A., Le Mével, H., Currenti, G., Williams-Jones, G., Tikoff, B., 2017a. 4D gravity changes at the Laguna del Maule volcanic field: magma induced stress changes facilitate mass addition. J. Geophys. Res., Solid Earth 122, 3179–3196. https://doi.org/10.1002/2017JB014048.

Miller, C.A., Williams-Jones, G., Fournier, D., Witter, J., 2017b. 3D gravity inversion and thermodynamic modelling reveal properties of shallow silicic magma reservoir beneath Laguna del Maule, Chile. Earth Planet. Sci. Lett. 459, 14–27. https://doi.org/10.1016/j.epsl.2016.11.007.

Nash, W.P., Crecraft, H.R., 1985. Partition coefficients for trace elements in silicic magmas. Geochim. Cosmochim. Acta 49, 2309–2322. https://doi.org/10.1016/0016-7037(85)90231-5.

Newhall, C.G., Costa, F., Ratdomopurbo, A., Venezky, D.Y., Widiwijayanti, C., Win, N.T.Z., Tan, K., Fajiculay, E., 2017. WOVOdat – an online, growing library of worldwide volcanic unrest. J. Volcanol. Geotherm. Res. https://doi.org/10.1016/j.jvolgeores.2017.08.003.

Newhall, C.G., Punongbayan, R.S., 1996. Fire and Mud: Eruptions and Lahars of Mount Pinatubo, Philippines. University of Washington Press, Seattle.

Newman, S., Lowenstern, J.B., 2002. Volatile Calc: a silicate melt–H_2O–CO_2 solution model written in Visual Basic for excel. Comput. Geosci. 28, 597–604. https://doi.org/10.1016/S0098-3004(01)00081-4.

Parks, M.M., Caliro, S., Chiodini, G., Pyle, D.M., Mather, T.A., Berlo, K., Edmonds, M., Biggs, J., Nomikou, P., Raptakis, C., 2013. Distinguishing contributions to diffuse CO_2 emissions in volcanic areas from magmatic degassing and thermal decarbonation using soil gas 222Rn–δ13C systematics: application to Santorini volcano, Greece. Earth Planet. Sci. Lett. 377–378, 180–190. https://doi.org/10.1016/j.epsl.2013.06.046.

Parmigiani, A., Faroughi, S., Huber, C., Bachmann, O., Su, Y., 2016. Bubble accumulation and its role in the evolution of magma reservoirs in the upper crust. Nature. https://doi.org/10.1038/nature17401.

Patiño Douce, A.E., Beard, J.S., 1995. Dehydration-melting of biotite gneiss and quartz amphibolite from 3 to 15 kbar. J. Petrol. 36, 707–738.

Pistolesi, M., Isaia, R., Marianelli, P., Bertagnini, A., Fourmentraux, C., Albert, P.G., Tomlinson, E.L., Menzies, M.A., Rosi, M., Sbrana, A., 2016. Simultaneous eruptions from multiple vents at Campi Flegrei (Italy) highlight new eruption processes at calderas. Geology 44, 487–490. https://doi.org/10.1130/G37870.1.

Ponader, C.W., Brown, G.E., 1989. Rare earth elements in silicate glass/melt systems: II. Interactions of La, Gd, and Yb with halogens. Geochim. Cosmochim. Acta 523, 2905–2914.

Putirka, K., 2016. Amphibole thermometers and barometers for igneous systems, and some implications for eruption mechanisms of felsic magmas at arc volcanoes. Am. Mineral. 101, 841–858. https://doi.org/10.2138/am-2016-5506.

Rapp, R.P., Watson, E.B., 1995. Dehydration melting of metabasalt at 8–32 kbar: implications for continental growth and crust-mantle recycling. J. Petrol. 36, 891–931.

Rea, J.C., 2009. The Petrology and Geochemistry of Volcán Callaqui. Senior Honors Thesis. Wesleyan University.

Rollinson, H., 1993. Using Geochemical Data. Longman Group, UK.

Rubin, A.E., Cooper, K.M., Till, C.B., Kent, A.J.R., Costa, F., Bose, M., Gravley, D., Deering, C., Cole, J., 2017. Rapid cooling and cold storage in a silicic magma reservoir recorded in individual crystals. Science 356, 1154–1156. https://doi.org/10.1126/science.aam8720.

Self, S., Blake, S., 2008. Consequences of explosive supereruptions. Elements 4, 41–46. https://doi.org/10.2113/GSELEMENTS.4.1.41.

Sherrod, D.R., Scott, W.E., Stauffer, P.H., 2008. A volcano rekindled: the renewed eruption of Mount St. Helens, 2004–2006. United States Geological Survey Professional Paper 1750.

Shinohara, H., 2008. Excess degassing from volcanoes and its role on eruptive and intrusive activity. Rev. Geophys. 46, 1–31. https://doi.org/10.1029/2007RG000244.

Shinohara, H., Witter, J.B., 2005. Volcanic gases emitted during mild Strombolian activity of Villarrica volcano, Chile. Geophys. Res. Lett. 32, 1–5. https://doi.org/10.1029/2005GL024131.

Singer, B.S., Andersen, N.L., Le Mével, H., Feigl, K.L., DeMets, C., Tikoff, B., Thurber, C.H., Jicha, B.R., Cardona, C., Cordova, L., Gil, F., Unsworth, M.J., Williams-Jones, G., Miller, C., Fierstein, J., Hildreth, W., Vazquez, J., Le Mevel, H., Feigl, K.L., DeMets, C., Tikoff, B., Thurber, C.H., Jicha, B.R., Cardona, C., Cordova, L., Gil, F., Unsworth, M.J., Williams-Jones, G., Miller, C., Fierstein, J., Hildreth, W., Vazquez, J., 2014. Dynamics of a large, restless, rhyolitic magma system at Laguna del Maule, southern Andes, Chile. GSA Today 24, 4–10. https://doi.org/10.1130/GSATG216A.1.

Singer, B.S., Costa, F., Herrin, J.S., Hildreth, W., Fierstein, J., 2016. The timing of compositionally-zoned magma reservoirs and mafic "priming" weeks before the 1912 Novarupta–Katmai rhyolite eruption. Earth Planet. Sci. Lett. 451, 125–137. https://doi.org/10.1016/j.epsl.2016.07.015.

Singer, B.S., Dungan, M., Layne, G., 1995. Textures and Sr, Ba, Mg, Fe, K, and Ti compositional profiles in volcanic plagioclase: clues to the dynamics of calc-alkaline magma chambers. Am. Mineral. 80, 776–798.

Singer, B.S., Hildreth, W., Vincze, Y., 2000. $^{40}Ar/^{39}Ar$ evidence for early deglaciation of the Central Chilean Andes. Geophys. Res. Lett. 27, 1663–1666.

Singer, B.S., Le Mével, H., Licciardi, J.M., Cordova, L., Tikoff, B., Garibaldi, N., Diefenbach, A.K., Andersen, N.L., Feigl, K.L., 2018. Integrating geomorphology, geochronology, and numerical modeling of 60-meter surface inflation to reveal Holocene growth of the silicic magma reservoir beneath Laguna del Maule, Chile, Presented at AGU Chapman Conference on Merging Geophysical, Petrochronologic, and Modeling Perspectives of Large Silicic Magma Systems, Quinamavida, Chile.

Singh, J., Johannes, W., 1996. Dehydration melting of tonalites. Part I. Beginning of melting. Contrib. Mineral. Petrol. 12, 16–25. https://doi.org/10.1007/s004100050203.

Smith, V.C., Blundy, J.D., Arce, J.L., 2009. A temporal record of magma accumulation and evolution beneath Nevado de Toluca, Mexico, preserved in plagioclase phenocrysts. J. Petrol. 50, 405–426. https://doi.org/10.1093/petrology/egp005.

Sparks, R.S.J., Self, S., Grattan, J., Oppenheimer, C., Pyle, D., Rymer, H., 2005. Super-Eruptions: Global Effects and Future Threats. Geological Society, London.

Sruoga, P., Elissondo, M., Rosas, M., Fierstein, J., Singer, B.S., Andersen, N.L., 2017. Cerro Barrancas, Laguna del Maule volcanic field, Chile: eruptive stratigraphy and hazard assessment. In: IAVCEI General Assembly, Portland, OR.

Till, C.B., Vazquez, J.A., Boyce, J.W., 2015. Months between rejuvenation and volcanic eruption at Yellowstone caldera, Wyoming. Geology 43, 695–698. https://doi.org/10.1130/G36862.1.

Tomiya, A., Miyagi, I., Saito, G., Geshi, N., 2013. Short time scales of magma-mixing processes prior to the 2011 eruption of Shinmoedake volcano, Kirishima volcanic group, Japan. Bull. Volcanol. 75, 1–19. https://doi.org/10.1007/s00445-013-0750-1.

Van Orman, J.A., Cherniak, D.J., Kita, N.T., 2014. Magnesium diffusion in plagioclase: dependence on composition, and implications for thermal resetting of the 26Al–26Mg early solar system chronometer. Earth Planet. Sci. Lett. 385, 79–88. https://doi.org/10.1016/j.epsl.2013.10.026.

Wallace, P.J., 2005. Volatiles in subduction zone magmas: concentrations and fluxes based on melt inclusion and volcanic gas data. J. Volcanol. Geotherm. Res. 140, 217–240. https://doi.org/10.1016/j.jvolgeores.2004.07.023.

Wallace, P.J., 2001. Volcanic SO_2 emissions and the abundance and distribution of exsolved gas in magma bodies. J. Volcanol. Geotherm. Res. 108, 85–106.

Wallace, P.J., Anderson, A.T., Davis, A.M., 1995. Quantification of pre-eruptive exsolved gas contents in silicic magmas. Nature 377, 612–616.

Waters, L.E., Lange, R.A., 2015. An updated calibration of the plagioclase-liquid hygrometer-thermometer applicable to basalts through rhyolites. Am. Mineral. 100, 2172–2184. https://doi.org/10.2138/am-2015-5232.

Watt, S.F.L., Pyle, D.M., Mather, T.A., Naranjo, J.A., 2013. Arc magma compositions controlled by linked thermal and chemical gradients above the subducting slab. Geophys. Res. Lett. 40, 2550–2556. https://doi.org/10.1002/grl.50513.

Wespestad, C.E., 2017. Surface Wave Tomography of Laguna del Maule Volcanic Field Using Ambient Noise and Regional Earthquakes. Masters Thesis. University of Wisconsin-Madison.

Wilson, C.J.N., 2017. Volcanoes: characteristics, tipping points, and those pesky unknown unknowns. Elements 13, 41–46. https://doi.org/10.2113/gselements.13.1.41.

Wolff, J.A., Ellis, B.S., Ramos, F.C., Starkel, W.A., Boroughs, S., Olin, P.H., Bachmann, O., 2015. Remelting of cumulates as a process for producing chemical zoning in silicic tuffs: a comparison of cool, wet and hot, dry rhyolitic magma systems. Lithos 236–237, 275–286. https://doi.org/10.1016/j.lithos.2015.09.002.